Accuracy and robustness of ODO/NHC measurement models for wheeled robot positioning

Liqiang Wang [a], Xiaoji Niu [a,b], Tisheng Zhang [a,*], Hailiang Tang [a], Qijin Chen [a]

[a] GNSS Research Center, Wuhan University, Wuhan 430072, China
[b] Artificial Intelligence Institute, Wuhan University, Wuhan 430072, China

ARTICLE INFO

ABSTRACT

The odometer (ODO) and non-holonomic constraint (NHC) are disturbed to a greater extent for wheeled robots by more serious vibrations and bumping compared to commercial cars. However, there have been few studies regarding the performances of different ODO/NHC measurement models for wheeled robot GNSS/INS positioning. In this study, the distance increment model was applied to not only the ODO measurement but also the NHC constraint. The measurement accuracy and robustness of this proposed 3D distance increment measurement versus conventional velocity measurement models were theoretically analyzed, and field tests evaluated in terms of positioning accuracy and robustness for wheeled robots. In the short-term (i.e., 1 min) GNSS outage test, the forward, lateral and vertical positioning drifts of the distance increment model decreased by 67 %, 15 %, and 39 %, respectively; and it also demonstrated superior robustness in the cases of carrier vibration, emergency stops, and passing speed bumps.

1. Introduction

With the continuous development of the robot industry, achieving low cost, continuity, high precision, and high robustness for wheeled robot positioning is required. The global navigation satellite system (GNSS) positioning technology provides locations that do not diverge with time. However, in scenarios with trees and high buildings blocking, where robots usually work, the GNSS positioning is severely degraded or even unavailable [1]. An inertial navigation system (INS) based on an inertial measurement unit (IMU) can output positioning results with high-frequency and continuity but diverges over time [2]. Although GNSS/INS integrated navigation solution utilizes the advantages of the two systems, a GNSS/INS system composed of a low-cost micro-electromechanical system (MEMS) IMU, which is commonly used in robots, can only maintain the positioning accuracy for a very short time when GNSS is unavailable [3,4]. Therefore, other sensors are needed for GNSS/MEMS IMU systems to provide continuous and accurate positioning in GNSS-denied environments.

A wheeled odometer (ODO), which naturally measures the distance increment during a period in the forward direction and also provides the forward speed [5], is an excellent auxiliary sensor for wheeled carriers. The motion of a wheeled carrier on a surface is governed by non-

holonomic constraint (NHC). When a wheeled carrier does not slip or skip, it only moves forward [6]. Therefore, NHC also provides speed information for wheeled carriers, i.e., the lateral and vertical speeds are zero. ODO and NHC are mostly employed together to constrain the carrier's three-dimensional (3D) speed. Besides the velocity constraint, NHC can be extended to constrain the vehicle's movement in lateral and vertical directions to zero. Therefore, NHC and ODO distance increment measurement can be employed together to provide 3D distance increment measurement. Thus, the velocity and distance increment measurement of ODO/NHC can be effective and economical auxiliary information for wheeled carriers.

ODO/NHC velocity measurements have been widely applied in land vehicle navigation [7–9] and railway tracking [10] to enhance GNSS/INS positioning accuracy. Among these studies, the authors of [7] fused the 3D velocity observation of the carrier with the MEMS IMU/GNSS integrated navigation system. The GNSS outage test proved that velocity assistance could significantly improve the positioning and heading accuracy of the system. The articles [11] and [12] converted the ODO/NHC measurements to the 3D displacement increment in the earth-centered-earth-fixed frame (e-frame) and local navigation frame (n-frame), respectively, and provided a 3D position constraint for the INS. In [13], the researchers proposed an INS/laser Doppler velocimeter

(LDV) integration algorithm. The sum of the velocity measurement, equivalent to the distance increment measurement, was employed to fully use the NHC/LDV measurements. In wheeled robot positioning, there are relatively few studies of ODO/NHC-assisted INS. Yousuf et al. [14] projected the ODO/NHC velocity using the heading angle measured by a gyroscope and fused the measurement with the INS for two-dimensional (2D) positioning. Zhang et al. [15] designed an ODO/NHC velocity auxiliary algorithm with steering angle compensation that can be applied to all-wheel steering robot positioning. The displacement increment in a 2D plane was calculated from the dual odometer in [16] for mobile robot localization. However, they did not fuse the ODO measurement with an INS.

Considering the different features of the two ODO/NHC measurements, a few researchers compared the navigation accuracy of the two measurement models. Ouyang et al. [17] analyzed ODO pulse increment and pulse speed measurement models based on a navigation-level IMU for land vehicles. The simulation and field test results showed that the pulse velocity measurement model outperformed the pulse increment model. However, in the pulse increment model, the authors employed distance increment measurement only in the forward direction, whereas still NHC velocity constraints in the lateral and vertical directions. Wu et al. [18] compared the velocity and displacement increment measurement models of a wheel-mounted MEMS IMU-based dead reckoning system. They obtained the virtual odometer measurement based on a wheel-mounted IMU rather than a wheel encoder. The test results indicated that the positioning accuracies of the two models were roughly equivalent, whereas the displacement increment model exhibited immunity to the lever arm error. Considering the different error characteristics between the virtual wheel-IMU odometer and a traditional wheel encoder measurement, this conclusion in [18] may not be suitable for the standard wheel-encoder odometer. Besides, authors in [17,18] compared ODO/NHC/IMU long-term dead reckoning accuracy. But the dead reckoning time of wheeled robots is usually short because GNSS mainly undergoes short-term outages in the work scene of wheeled robots.

The literature survey shows the ODO/NHC velocity and distance increment measurements have been applied and compared in land vehicle navigation by some researchers. Previous studies have drawn some conclusions on the two models for land vehicles in long-distance navigation. Although wheeled robots are also wheeled carriers, they yield more variable speed and more arbitrary trajectories than land vehicles. Besides, the short-term dead reckoning accuracy is more concerned for wheeled robots as GNSS signals interrupt only for a short time in their working place. Therefore, the above conclusions for land vehicles cannot be extended to wheeled robots. However, rare literature studied the positioning accuracy of the two ODO/NHC measurement models for wheeled robots. It is necessary to analyze the accuracy of the two models in wheeled robot navigation.

In addition, wheeled robots typically have a simple structure and an imprecise buffer system. As a result, they are more prone to significant vibrations and swings. When passing obstacles, such as a speed bump, wheeled robots will vibrate and jolt severely, which breaks their kinematic hypothesis. Therefore, the robustness of the ODO/NHC measurement model is equally significant for wheeled robot positioning. However, the robustness of the models has received little attention and research.

Based on the above consideration, we conducted the following research to analyze the positioning accuracy and robustness of the ODO/NHC velocity and distance increment measurement models for wheeled robot navigation. First, we constructed ODO/NHC velocity and distance increment measurement models in the carrier frame based on the GNSS/INS integration error state model. Then the ODO/NHC velocity and distance increment measurement errors in wheeled robots are analyzed. Additionally, adequate field tests were conducted on a mobile wheeled robot to evaluate the positioning accuracy in short-term GNSS outages and robustness of the two ODO/NHC measurement models. The main

contributions of this study are as follows:

- NHC is extended as a distance increment constraint, ODO/NHC distance increment measurement model for GNSS/INS integration is constructed in the carrier frame.
- The ODO speed and distance increment measurement accuracy is quantitatively studied, and the robustness of ODO/NHC velocity and distance increment measurement models are analyzed based on the motion characteristics of wheeled robots.
- Adequate field tests are conducted to evaluate the positioning accuracy of the ODO/NHC velocity and distance increment models, and dedicated tests are designed to evaluate the robustness of the two models.

The remainder of this paper is organized as follows. Section 2 constructs the two ODO/NHC measurement models and analyzes the errors of the two ODO/NHC auxiliary information. The field tests and data processing methods are described in Section 3. Section 4 presents and discusses the results of the field experiment. Finally, this paper is concluded in Section 5.

2. Methodology

This section presents the established coordinate system, describes the two ODO/NHC measurement models and analyzes their measurement errors. It is worth mentioning that the derived ODO/NHC measurement models in this study only apply to wheeled robots that comply with NHC, for example, wheeled robots under the Ackermann Motion model or Corner Steering Motion model [19].

The wheeled carrier in our experiments complies with the Corner Steering Motion model. As shown in Fig. 1, the carrier has six wheels, with two middle wheels non-steering. We obtained the equivalent odometer at the center of the non-steering axis by averaging the odometer measurements of the two middle wheels. We define the point at which the center of the non-steering axis is projected onto the ground as the origin of the vehicle frame (v-frame). The x-axis of the v-frame points in the forward direction of the vehicle, and the points in the y- and z-axes in the right and down directions, respectively. The b-frame denotes the IMU body frame, where the origin is located at the geometric center of the IMU. The positioning results are represented in the local navigation frame with the exact origin as the b-frame. The three axes points are in the north, east, and down directions, respectively. In addition, the IMU installation angles denote the rotational angles between the b- and v-frames, of which the direction cosine matrix (DCM) is expressed as C_b^v. The displacement between the origins of the b- and v-frames is the lever arm l_{bv}^b, which is measured in the b-frame.
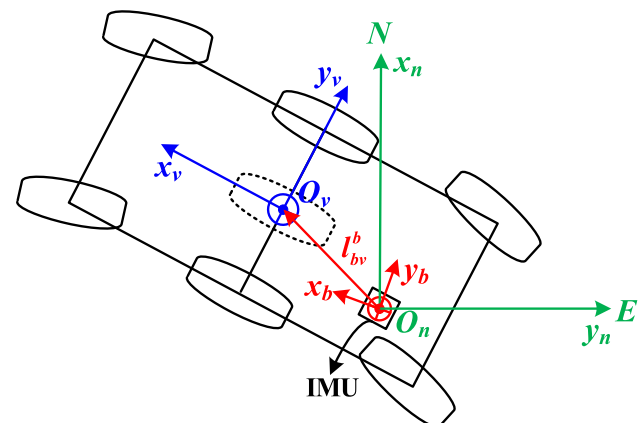

Fig. 1. Definition of the coordinate systems.

2.1. Error state model

The error-state Kalman filter, the most popular estimation method in GNSS/INS integration, is utilized in this study to fuse the measurements. We augment the sensor errors into the state vector with position error δr^n, velocity error δv^n, and attitude error θ when constructing the error state model of the Kalman filter. Generally, the IMU scale factor errors are absorbed in the bias errors and are difficult to estimate because the MEMS IMU usually has poor bias stability. Therefore, we only model the IMU bias errors (i.e., the gyroscope bias errors δb_g and accelerometer bias errors δb_a). The scale factor between the odometer pulse and vehicle motion information is difficult to measure accurately. Hence, we augment the scale factor error δk, as a system state to be estimated. The total system error state is constructed as.

$$\delta \boldsymbol{x} = \begin{bmatrix} \boldsymbol{\theta}^T & (\delta \boldsymbol{r}^n)^T & (\delta \boldsymbol{v}^n)^T & \delta \boldsymbol{b}_g^T & \delta \boldsymbol{b}_a^T & \delta k \end{bmatrix}^T \tag{1}$$

The attitude errors are defined as.

$$\widehat{\boldsymbol{C}}_b^n = \boldsymbol{C}_b^n (\boldsymbol{I} - (\boldsymbol{\theta} \times)) \tag{2}$$

where θ is the rotation vector corresponding to the attitude error, $\boldsymbol{C}_b^n$ is the DCM of the true attitude, and $\widehat{\boldsymbol{C}}_b^n$ is the DCM of the estimated attitude.

Other state errors are defined as.

$$\delta \boldsymbol{x} = \boldsymbol{x} - \widehat{\boldsymbol{x}} \tag{3}$$

where δx is the error state vector, x is the true state, and $\widehat{x}$ denotes the estimated state with the error.

First, we establish an error differential equation of the state vector to propagate the error state. The error differential equations of position, velocity, and attitude are expressed as.

$$
\begin{aligned}
\delta \dot{\boldsymbol{r}}^n &= \boldsymbol{F}_{rr} \delta \boldsymbol{r}^n + \delta \boldsymbol{v}^n \\
\delta \dot{\boldsymbol{v}}^n &= -\boldsymbol{C}_b^n \delta \boldsymbol{f}^b - \boldsymbol{C}_b^n (\boldsymbol{f}^b \times) \boldsymbol{\theta} - (2\boldsymbol{\omega}_{ie}^n + \boldsymbol{\omega}_{en}^n) \times \delta \boldsymbol{v}^n + \boldsymbol{v}^n \times (2\delta \boldsymbol{\omega}_{ie}^n + \delta \boldsymbol{\omega}_{en}^n) + \delta \boldsymbol{g}_l^n \\
\dot{\boldsymbol{\theta}} &= -(\boldsymbol{\omega}_{ib}^b \times) \boldsymbol{\theta} - \delta \boldsymbol{\omega}_{ib}^b + \boldsymbol{C}_n^b (\boldsymbol{\omega}_{ie}^n + \boldsymbol{\omega}_{en}^n)
\end{aligned}
\tag{4}
$$

where ω_{ie}^n and ω_{en}^n denote the earth's rotational angular velocity and the angular velocity of the n-frame relative to the e-frame, respectively, g_l^n is the gravitational acceleration vector, which can be calculated using the latitude and height [20], f^b and ω_{ib}^b are the acceleration and angular velocity of the IMU, respectively, and $\delta \cdot$ is the corresponding state error. In this study, the acceleration error δf^b and angular velocity error $\delta \omega_{ib}^b$ are equivalent to the bias error δb_a and δb_g, respectively. $\boldsymbol{F}_{rr}$ is the coefficient matrix of the position error, the components of which are as.

$$
\boldsymbol{F}_{rr} = \begin{bmatrix}
-\dfrac{v_D}{R_M + h} & 0 & \dfrac{v_N}{R_M + h} \\[2ex]
\dfrac{v_E \tan\varphi}{R_N} + h & -\dfrac{v_D + v_N \tan\varphi}{R_N + h} & \dfrac{v_E}{R_N + h} \\[2ex]
0 & 0 & 0
\end{bmatrix}
\tag{5}
$$

where v_N, v_E, and v_D are the velocity of the IMU in the three directions of the n-frame, φ is the local latitude, h is the height, and R_M and R_N are the Meridian and Mao unitary radii, respectively.

We construct the sensor error differential equation based on the characteristics of the sensor. The IMU bias errors are modeled as a first-order Gaussian Markov process because they changed slowly. The odometer scale error is modeled as a random walk process, as it would vary on changeable working conditions. The error differential equations of IMU bias errors and odometer scale error are defined as.

$$
\begin{aligned}
\delta \dot{\boldsymbol{b}}_g &= -\delta \boldsymbol{b}_g / T_g + \boldsymbol{\omega}_g \\
\delta \dot{\boldsymbol{b}}_a &= -\delta \boldsymbol{b}_a / T_a + \boldsymbol{\omega}_a \\
\delta \dot{k} &= \omega_{odo}
\end{aligned}
\tag{6}
$$

where T_g and T_a are the error correlation times of the gyroscope bias and accelerometer bias, respectively, ω_g and ω_a are the drive white noise of the bias error models, and ω_{odo} is the drive white noise of the odometer scale error.

In the Kalman filter, the discrete error state propagation can be expressed as.

$$\delta \boldsymbol{x}_k = \boldsymbol{\Phi}_{k,k-1} \delta \boldsymbol{x}_{k-1} + \boldsymbol{\omega}_{k-1} \tag{7}$$

where $\delta \boldsymbol{x}_{k-1}$ is the error state at t_{k-1}, $\boldsymbol{\Phi}_{k,k-1}$ is the state transition matrix from t_{k-1} to t_k, and ω_{k-1} is the system noise during state propagation with the covariance of $\boldsymbol{Q}_{k-1}$.

The discrete measurement equation of the Kalman filter is.

$$\boldsymbol{z}_k = \boldsymbol{H}_k \delta \boldsymbol{x}_k + \boldsymbol{v}_k \tag{8}$$

where z_k is the measurement innovation obtained by subtracting the measurement state from the estimated state, v_k is the measurement noise, and $\boldsymbol{H}_k$ is the measurement matrix. Subsequently, we will derive the ODO/NHC velocity and distance increment measurement equations.

2.2. Velocity measurement model

It is necessary to project the INS velocity under the n-frame to the v-frame to calculate ODO/NHC measurement innovation. The IMU installation angles and odometer lever arm are required for the velocity projection. We treat the installation angles and lever arm as constant values to reduce the influence of uncertainty factors on navigation accuracy. The installation angles were estimated using the method proposed in [21]. Based on the required lever-arm accuracy investigated in [22], the lever arm was measured by a tape, which is sufficiently accurate. We multiply the odometer scale with the estimated vehicle velocity to establish the measurement equation intuitively. The estimated vehicle velocity is.

$$\widehat{\boldsymbol{v}}^v = \widehat{\boldsymbol{K}} \widehat{\boldsymbol{C}}_n^v \left(\widehat{\boldsymbol{C}}_n^b \widehat{\boldsymbol{v}}^n + \left(\widehat{\boldsymbol{\omega}}_{ib}^b - \widehat{\boldsymbol{C}}_n^b \widehat{\boldsymbol{\omega}}_{in}^n \right) \times \boldsymbol{l}^b \right) \tag{9}$$

where $\boldsymbol{K} = diag[1 + k \quad 1 \quad 1]$ is the scale factor matrix of the velocity in the v-frame. The second and third diagonal elements of K are set to 1 because there are no scale errors in the lateral and vertical speeds of the carrier.

The ODO/NHC measurement velocity in the v-frame is.

$$\widetilde{\boldsymbol{v}}^v = \begin{bmatrix} \widetilde{v}_{odo} & 0 & 0 \end{bmatrix}^T = \boldsymbol{v}^v - \boldsymbol{e}_v \tag{10}$$

where $\widetilde{v}_{odo}$ is the speed measurement of the odometer, v^v is the truth vehicle velocity in the v-frame and e_v is the ODO/NHC velocity measurement error.

The velocity measurement innovation is calculated as:

$$\delta \boldsymbol{v}^v = \widehat{\boldsymbol{v}}^v - \widetilde{\boldsymbol{v}}^v \tag{11}$$

Performing error perturbation on $\widehat{v}^v$ and ignoring the small second-order error, we obtain the below velocity measurement equation as.

$$
\begin{aligned}
\boldsymbol{z}_v &= \boldsymbol{H}_v \delta \boldsymbol{x} + \boldsymbol{e}_v \\
&= -\boldsymbol{e}_1 \boldsymbol{C}_b^v \left(\boldsymbol{C}_b^v \boldsymbol{v}^n + (\boldsymbol{\omega}_{nb}^b \times) \boldsymbol{l}^b \right) \delta k - K \boldsymbol{C}_b^v \left[(\boldsymbol{C}_b^v \boldsymbol{v}^n) \times \right] \boldsymbol{\theta} - K \boldsymbol{C}_b^v \boldsymbol{C}_n^b \delta \boldsymbol{v}^n \\
&\quad - K \boldsymbol{C}_b^v (\boldsymbol{l}^b \times) \delta \boldsymbol{b}_g - K \boldsymbol{C}_b^v (\boldsymbol{l}^b \times) \left[(\boldsymbol{C}_n^b \boldsymbol{\omega}_{in}^n) \times \right] \boldsymbol{\theta} - K \boldsymbol{C}_b^v (\boldsymbol{l}^b \times) \boldsymbol{C}_n^b \delta \boldsymbol{\omega}_{in}^n + \boldsymbol{e}_v
\end{aligned}
\tag{12}
$$

where $\boldsymbol{e}_1 = diag[1 \quad 0 \quad 0]$, $\boldsymbol{\omega}_{nb}^b = \boldsymbol{\omega}_{ib}^b - \boldsymbol{C}_n^b \boldsymbol{\omega}_{in}^n$, $\boldsymbol{H}_v$ is the velocity measurement matrix. $\delta \boldsymbol{\omega}_{in}^n = \delta \boldsymbol{\omega}_{ie}^n + \delta \boldsymbol{\omega}_{en}^n$ is generally negligible for low-speed carriers. Thus, we get the expression of H_v as.

$$
\begin{aligned}
\boldsymbol{H}_v = \big[& 0_{3\times3}, \quad -K\boldsymbol{C}_b^v \boldsymbol{C}_n^b, \quad -K\boldsymbol{C}_b^v \left[(\boldsymbol{C}_b^v \boldsymbol{v}^n) \times \right] - K\boldsymbol{C}_b^v (\boldsymbol{l}^b \times) \left[(\boldsymbol{C}_n^b \boldsymbol{\omega}_{in}^n) \times \right], \\
& -K\boldsymbol{C}_b^v (\boldsymbol{l}^b \times), \quad 0_{3\times3}, \quad -\boldsymbol{e}_1 \boldsymbol{C}_b^v \left(\boldsymbol{C}_n^b \boldsymbol{v}^n + (\boldsymbol{\omega}_{nb}^b \times) \boldsymbol{l}^b \right) \big]
\end{aligned}
\tag{13}
$$

We can then update the state vector using the ODO/NHC velocity measurements.

2.3. Distance increment measurement model

The distance increment measurements are the accumulated distances in the three directions of the vehicle frame during a given period. Instead of projecting ODO/NHC measurement to n-frame or e-frame, we construct the distance increment model in the vehicle's three directions, which split ODO/NHC measurement error and attitude error. Different from the pulse increment model in [17], we extend NHC from speed constraint to distance increment constraint, which reduces the random speed noise in the vehicle's lateral and vertical directioins.

The ODO/NHC distance increment measurement model in this study is derived based on the summed measurement method [13,23]. We consider the velocity between two consecutive epochs to vary linearly since the IMU data rate is usually high enough. Then, the estimated distance increments in the three directions of the v-frame from t_{k-1} to t_k can be derived as:

$$\Delta \widehat{s}_k^v = \int_{t_{k-1}}^{t_k} \widehat{v}^v(t)dt \approx \widehat{v}_{k-1/2}^v \Delta t_k \tag{14}$$

where, $\Delta t_k = t_k - t_{k-1}$ and $\widehat{v}_{k-1/2}^v = \left(\widehat{v}_{k-1}^v + \widehat{v}_k^v\right)/2$.

Assuming that there are N epochs during the update period, the estimated distance increments from t_{k-N+1} to t_k are.

$$\Delta \widehat{s}^v = \int_{t_{k-N+1}}^{t_k} \widehat{v}^v dt = \sum_{i=k-N+1}^{k} \Delta \widehat{s}_i^v \approx \sum_{i=k-N+1}^{k} \frac{1}{2}\left(\widehat{v}_{i-1}^v + \widehat{v}_i^v\right)\Delta t_i \tag{15}$$

The ODO/NHC distance increment measurement in three directions is given by.

$$\Delta \widetilde{s}^v = \left[\Delta \widetilde{s}_{odo}\ 0\ 0\right]^T = \Delta s^v - e_s \tag{16}$$

where $\Delta \widetilde{s}_{odo}$ is the distance increment measurement of the odometer, Δs^v is the truth distance increments in the three directions of the vehicle and e_s is the ODO/NHC distance increment measurement error.

The measurement innovation of the ODO/NHC distance increment can be calculated as.

$$\delta \Delta s^v = \Delta \widehat{s}^v - \Delta \widetilde{s}^v = \sum_{i=k-N+1}^{k} \delta \Delta s_i^v + e_s \tag{17}$$

where $\delta \Delta s_i^v$ is the estimated distance increment error from t_{i-1} to t_i. We derive $\delta \Delta s_i^v$ from the estimated vehicle velocity as.

$$\delta \Delta s_i^v = \frac{1}{2}\left(\widehat{v}_{i-1}^v - v_{i-1}^v + \widehat{v}_i^v - v_i^v\right)\Delta t_i \tag{18}$$

Similar to the velocity measurement equation, we ignore the small second-order error and obtain the distance increment measurement equation from (17), as shown below:

$$z_s = \frac{1}{2}\sum_{i=k-N+1}^{k}\left(H_{v,i}\Delta t_i \delta x_i + H_{v,i-1}\Delta t_i \delta x_{i-1}\right) + e_s$$
$$= \frac{1}{2}H_{v,k-N}\Delta t_{k-N+1}\delta x_{k-N} + \sum_{i=k-N+1}^{k}\left(H_{v,i}\Delta t_i \delta x_i\right) - \frac{1}{2}H_{v,k}\Delta t_k \delta x_k + e_s \tag{19}$$

To separate the distance increment measurement and the states at the previous epochs, we build the transformation between t_i and t_k by the state transition matrix. Transforming (7), we yield $\delta x_{k-1} = \Phi_{k,k-1}^{-1}(\delta x_k - \omega_{k-1})$. To simplify the measurement model, we ignore the system noise during state transition. Then, the error state δx_i can be expressed with the current error state δx_k as.

$$\delta x_i = \Phi_{k,i}^{-1}\delta x_k$$
$$\Phi_{k,i} = \Phi_{k,k-1}\cdots\Phi_{i+1,i} \tag{20}$$

Substituting (20) into (19), we obtain the distance increment measurement equation as.

$$z_s = \frac{1}{2}H_{v,k-N}\Delta t_{k-N+1}\Phi_{k,k-N}^{-1}\delta x_k + \sum_{i=k-N+1}^{k} H_{v,i}\Delta t_i \Phi_{k,i}^{-1}\delta x_k - \frac{1}{2}H_{v,k}\Delta t_k \delta x_k + e_s \tag{21}$$

which is only a function of the current state. We mark the distance increment measurement matrix as H_s, which is.

$$H_s = \frac{1}{2}H_{v,k-N}\Delta t_{k-N+1}\Phi_{k,k-N}^{-1} + \sum_{i=k-N+1}^{k} H_{v,i}\Phi_{k,i}^{-1}\Delta t_i - \frac{1}{2}H_{v,k}\Delta t_k \tag{22}$$

Then, we can perform the state update process based on the distance increment measurement matrix.

2.4. Measurement quality analysis

2.4.1. Accuracy analysis

The wheel odometer is innately an encoder that counts the pulse number generated by the carrier movement [24]. Assuming that the counting pulse increment is ΔN during the sample period T, we can derive the odometer velocity as.

$$\widetilde{v}_{odo} = \frac{\pi D}{P}\frac{(\Delta N + \delta p)}{T} \tag{23}$$

where D is the wheel diameter, P, which is called the resolution, is the pulse number during one wheel revolution, and δp is the error of the odometer pulses. In this study, the wheeled robot was equipped with an odometer with a wheel diameter of 0.15 m, a resolution of 800, a sampling rate of 200 Hz, and a pulse measurement error of 1. Using (23), we obtain the odometer measurement speed error as approximately 0.118 m/s, a considerable quantization error. The assumption of constant acceleration is commonly used during update intervals to reduce the quantization noise of the odometer in engineering applications [17]. We take the linear extrapolation method as the example in this study to analyze the measurement error.

Linear extrapolation assumes that speed varies linearly over the update interval. This method is divided into two steps: i) calculating the mean speed of the first and second half intervals, and ii) extrapolating the current speed. If the half interval is 0.5 s, the average speed measurement error reduces to 0.0012 m/s, which is significantly lower than the error measured from one sample epoch. Then, we adopt the error modeling method in [17] to quantitatively analyze the speed error and distance increment error of the odometer. In other words, the pulse measurement error is modeled as a uniform distribution between $[0, 1)$ and the variance of $var(\delta p) = 1/12$. In addition, the pulse measurement errors at different times are independent of each other.

The pulse counts of $t = 0s$, $0.5s$, and $1s$ are denoted as $\widetilde{s}_0$, $\widetilde{s}_{0.5}$, and $\widetilde{s}_1$, respectively. The extrapolation speed at $t = 1s$ can be derived from the pulse counts in the last second as.

$$\widetilde{v}_{odo} = \frac{\pi D}{P}\left(3\widetilde{s}_1 - 4\widetilde{s}_{0.5} + \widetilde{s}_0\right) \tag{24}$$

The extrapolation speed error is calculated as:

$$e_v = \frac{\pi D}{P}(3\widetilde{s}_1 - 4\widetilde{s}_{0.5} + \widetilde{s}_0) - \frac{\pi D}{P}(3s_1 - 4s_{0.5} + s_0)$$
$$= \frac{\pi D}{P}(3\delta p_1 - 4\delta p_{0.5} + \delta p_0) \tag{25}$$

where, δp_0, $\delta p_{0.5}$, and δp_1 are the pulse measurement error at $t = 0s$, $0.5s$, and $1s$, respectively. Using the covariance of the pulse measurement error, we obtain the standard deviation (STD) of the speed error as $\sigma(e_v) \approx 1.47\pi D/P$ m/s.

The distance increment measurement error is only related to the pulse error at $t = 0s$ and $1s$, and is calculated as.

$$e_s = \frac{\pi D}{P}\left(\widetilde{s}_1 - \widetilde{s}_0\right) - \frac{\pi D}{P}(s_1 - s_0) = \frac{\pi D}{P}(\delta p_1 - \delta p_0) \tag{26}$$

The STD of distance increment measurement error is $\sigma(e_s) \approx 0.41\pi D/P$ m.

We convert the distance increment measurement error in one second to the average speed error, for which the STD is $\dot{\sigma}(e_s) = 0.41\pi D/P$ m/s. It can be derived that the odometer distance increment measurement error decreases by 72 % compared with the speed measurement error.

The lateral and vertical speed errors are mainly caused by the carrier vibration, and we model them as random white noise. Thus, the measurement error will decrease by $\sqrt{1/T}$ times theoretically when extended to distance increment. In this study, the theoretical error decrease of lateral and vertical distance increment is 93 %.

2.4.2. Robustness analysis

Although the linear extrapolation method in (24) effectively reduces the speed quantization error, this method inevitably introduces additional speed errors when the velocity linearity assumption is not satisfied. The speed linearity assumption is severely broken when the vehicle speed varies drastically, the speed linearity assumption is severely broken, and the extrapolation speed error increases significantly. In contrast, nonlinear speed changes do not significantly affect the accuracy of the distance increment.

Compared to common land vehicles, such as commercial cars, wheeled robots usually have tiny wheels and poor shock absorption designs. Moving robots may suffer from serious vibrations, which add additional instantaneous speed at the location of the IMU. The odometer cannot measure the speed vibration because the wheels, which are in contact with the ground, are not affected by the vibration of the carrier. Therefore, the odometer speed measurement error increases, resulting in a poor speed auxiliary effect. In contrast, the moving distance of the entire robot is not significantly affected by the vibration. Therefore, the forward distance increment accuracy can be guaranteed under such vibrations. Similarly, the conventional speed constraints of the NHC degrade when the lateral and vertical speeds of the robot are vibrated by the carrier jitter and bump. However, the lateral and vertical distance increment constraints correspond more to the actual movement (i.e., the macro movement distance is zero).

Based on the above analysis, the measurement at the distance increment level is not sensitive to drastic changes in carrier speed. It can also deal more robustly with the jitter and bump of the carrier. Therefore, we expect the ODO/NHC distance increment measurements to exhibit more robust and accurate positioning performance.

3. Field tests

Field tests were conducted on a mobile wheeled robot to evaluate the performance of the two measurement models in real applications. This section describes the test detail and our data processing method.

3.1. Test description

We conducted field tests on the six-wheeled robot shown in Fig. 2(a), in which the middle two wheels were non-steering wheels when driving. The average of the encoder pulses from the two middle wheels is considered the equivalent odometer measurement at the center of the non-steering axes. The odometer and wheel parameters are described in Section 2.4.1. Four GNSS/INS integrated navigation modules (INS-Probe) were mounted to collect four measurements of ADIS16465 (quasi-tactical-grade MEMS IMU). One INS-Probe synchronously collected odometer measurements and GNSS RTK positioning results. In addition, one INS-Probe was installed on the robot tower, and the remaining INS-Probes were distributed on the board. The IMUs and odometer data were sampled at 200 Hz, and the GNSS results were sampled at 1 Hz. The navigation-grade IMU Leador-A15 was used as the ground truth. Table 1 lists the main parameters of the two IMUs.

Fig. 2 (b) illustrates the driving track of the robot under open-sky
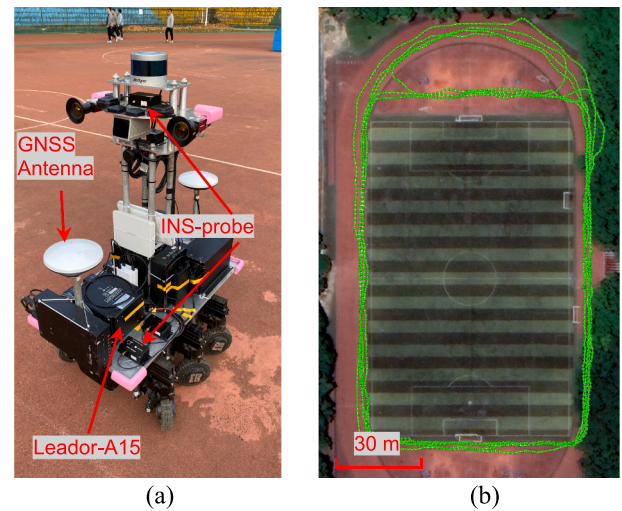

Fig. 2. Field test robot and trajectory.

conditions. The open area ensured centimeter-level GNSS real-time kinematic (RTK) positioning. The robot was firstly stationary for approximately 400 s such that the reference truth system (Leador-A15) could perform a precise initial alignment. Subsequently, the robot moved along the trajectory shown in the figure, accompanied by acceleration, deceleration, and turning. We conducted seven tests in this scene (denoted as A–G groups) to ensure that the evaluation results were representative and statically sufficient.

3.2. Accuracy comparison method

3.2.1. ODO/NHC measurement accuracy

In the field test, the velocity in the v-frame derived from the high-precision reference frame was considered the real velocity. Subsequently, the real distance increments of each second were calculated. Note that the real velocity and distance increment in the lateral and vertical directions were not zero because of the carrier's vibration in the real test. Then, we calculated the ODO/NHC measurement error.

We could not directly compare the ODO/NHC velocity measurement error and distance increment measurement error cause they have different physical meanings. Therefore, we converted the distance increment errors within 1 s to average speed errors, which were compared with the ODO/NHC velocity measurement errors. The root mean square (RMS) values of the measurement errors were calculated and employed as the accuracy criteria for the velocity and distance increment measurements.

3.2.2. Positioning accuracy

The reference trajectory was acquired by fusing the RTK positioning results and the IMU measurements of Leador-A15 in a Rauch-Tung-Striebel smoother. We adopted a GNSS outage test to evaluate the positioning accuracy of the two ODO/NHC measurement models [25]. GNSS outage occurred after the IMU bias errors fully converged. Considering the GNSS outage time in the robot work scene, we artificially interrupted the GNSS signal for 60 s every 180 s. We also postponed the outage start time by 60 s and 120 s to get more outage test

Table 1
Technique parameters of the Two IMUs.

IMU	ADIS16465	Leador A15
Gyro bias stability [deg/h]	50	0.02
Gyro white noise [$deg/\sqrt{h}$]	0.1	0.003
Accel bias stability [$mGal$]	50	15
Accel white noise [$m/s/\sqrt{h}$]	0.1	0.03

samples. For every outage test, we calculated the RMS values of the position drifts in the forward, lateral, and vertical directions during all periods of GNSS outage. Subsequently, the RMS values of the position error were considered as the positioning accuracy evaluation criteria of the two ODO/NHC measurement models.

4. Results and discussion

4.1. Measurement accuracy analysis

We first evaluated the error in the ODO/NHC velocity and distance increment measurements. The odometer speed was obtained using the linear extrapolation method described in Section 2.4.1. Using the accuracy comparison method described in Section 3, we calculated the seven tests' ODO/NHC velocity and distance increment measurement accuracy. The ODO/NHC measurement error of Group B is shown in Fig. 3. Furthermore, we counted the RMS values of the seven tests' measurement error, and the comparison between the two measurements is shown in Table 2. Note that we replace the distance increment model with Distance Model in all tables for simplicity. The error decrease in Table 2 denotes the speed error decrease of the distance increment measurement compared with the velocity measurement.

It is evident from Fig. 3 and Table 2 that the distance increment measurement errors in the forward and vertical directions are significantly smaller than the velocity measurement errors. The error decreases are 89 % and 86 %, respectively. In the forward direction (i.e., the odometer measurement), the error decrease was larger than the theoretical analysis of 72 %. This reflects the influence of the speed nonlinearity and carrier vibration on the odometer measurement speed. In the vertical direction, the error decrease is consistent with our theoretical analysis.

However, in the lateral direction, the error decrease is quite different from the theoretical analysis and exhibits no significant improvement compared with that in the other two directions. The derived lateral speed and distance increment in GNSS/INS integration system are related to the lever arm and heading angle. Moreover, the lever arm error and heading angle error affect both the speed and distance increment measurements. Therefore, the distance increment measurement error in the lateral direction is not significantly improved than the velocity measurement error. Although the error caused by the carrier

Table 2
Error of the two ODO/NHC measurements.

Measurement Error	Velocity Model [m/s]	Distance Model [m/s]	Error Decrease [%]
Forward	0.031	0.0035	89
Lateral	0.018	0.014	25
Vertical	0.0094	0.0013	86

vibration is not manifested, the lateral distance increment measurement error decreases by 25 %.

4.2. Positioning accuracy analysis

We employed the accuracy comparison method described in Section 3.2 to calculate the positioning error of the two ODO/NHC measurement models. The theoretical ODO/NHC measurement noise is usually smaller than the actual measurement error due to the complex situation in a field test. Therefore, it is necessary to adjust the measurement noise parameters appropriately based on carrier motion characteristics. Aiming at a minimum position error, we optimized the noise parameters of the two measurement models with the A, D, and G group data. The positioning errors of the two models in one outage test are shown in Fig. 4. Then, the optimized noise parameters were employed in the GNSS outage tests of the remaining four groups of data. Subsequently, we calculated the RMS position error and evaluated the positioning accuracy of the two ODO/NHC measurement models. Table 3 lists the position errors of the two measurement models. The error decrease in the following tables denotes the positioning error decrease of the distance increment measurement model compared with the velocity measurement model.

It is apparent from Table 3 that the position errors derived from the distance increment model are smaller than those of the velocity measurement model in the three directions of the v-frame. Statistically, the positioning errors of the distance increment model decreased by 67 %, 15 %, and 39 %, respectively. In the lateral direction, the error decrease is significantly smaller than in the other two directions, consistent with the measurement accuracy analysis. We reason that the large attitude error in field tests, which is caused by the unmodeled sensor error, the installation angle residual error, etc., results in a large positioning error
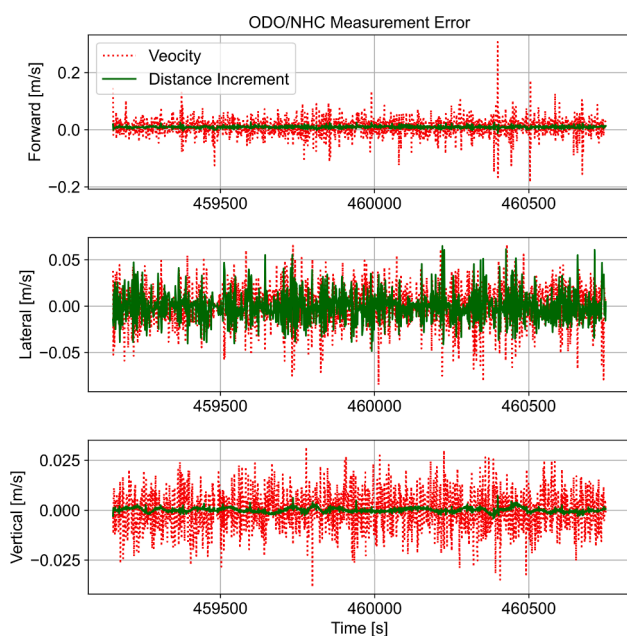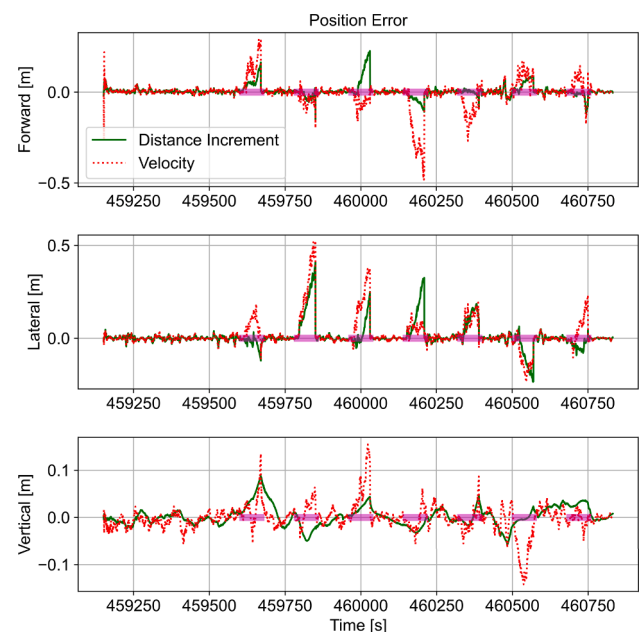

Fig. 3. ODO/NHC measurement error of Group B.

Fig. 4. Position Error of one outage test. The pink bands indicate GNSS outages.

Table 3
Position Errors of the Four Groups Field Test.

Test Group	Velocity Model [m]			Distance Model [m]			Error Decrease [%]		
	Forward	Lateral	Vertical	Forward	Lateral	Vertical	Forward	Lateral	Vertical
B	0.257	0.270	0.074	0.107	0.220	0.046	58	18	38
C	0.225	0.296	0.085	0.074	0.228	0.047	67	23	45
E	0.252	0.267	0.083	0.080	0.266	0.050	68	0	39
F	0.264	0.391	0.091	0.068	0.324	0.059	74	17	35
RMS	**0.250**	**0.310**	**0.083**	**0.084**	**0.262**	**0.051**	**67**	**15**	**39**

in the lateral direction. And it also leads to a slight error decrease of the distance increment model in the field tests. Nonetheless, the error decrease in the lateral and vertical directions verified the accuracy advantage of extending NHC to a distance increment constraint.

Then, we calculated the RMS values of the position error during all the 60 s GNSS outage periods. The position error drift curves of the two measurement models are shown in Fig. 5. In Fig. 5, the forward, lateral and vertical position errors derived from the velocity model are always higher than those derived from the distance increment model throughout the GNSS outage period. Moreover, the forward and vertical position errors of the velocity model diverge faster as the GNSS outage time increases. In the lateral direction, the positioning errors of the two ODO/NHC models increase at approximately the same rate when the GNSS outage time is longer than 25 s. This is because the accumulated INS errors, particularly the heading angle error, play an essential role in the lateral position error as the outage time increases. The two ODO/NHC measurement models rely on the accuracy of the INS heading angle, which diverges during GNSS outages. Therefore, the difference between the two models is gradually covered by the increasing attitude error. Consequently, the error decrease of the distance increment model in the lateral direction becomes unobvious when GNSS outages 60 s.

4.3. Robustness test and analysis

This section describes three dedicated tests designed to evaluate the robustness of the velocity and distance increment models. The first test analyzed the influence of carrier vibration on the performance of the two models. Then, an emergency stop test was conducted to simulate the scenario where the speed linearity assumption was broken. Finally, the passing speed bump experiment was conducted to simulate the scene in

which the IMU installation angles and lever arm change briefly.

4.3.1. Carrier vibration test

When the robot moves, the IMU installed on the tower vibrates more severely than the IMU installed on the board, particularly horizontally. Therefore, we compare the position errors of the IMUs installed on the tower and board to analyze the impact of carrier vibration on the two models.

First, we used the IMU v-frame velocity STD during 1 s to describe the vibration and verify that the robot tower vibrates more severely. The RMS of the velocity STD was calculated to compare the carrier vibrations at different positions. We only consider epochs where the forward speed STD is smaller than 0.5 m/s in this study to avoid the contribution of acceleration and deceleration to the forward speed STD. Table 4 lists the velocity STD of the IMUs installed on the tower (T17) and the board (H4).

In Table 4, the velocity STD demonstrates that the IMU installed on the tower (T17) yields greater speed vibration in the forward and lateral directions than that on the board (H4), which is consistent with our analysis. Then, we counted the position errors of T17 and H4 in the GNSS outage tests as shown in Table 5.

The position error decrease of the distance increment model in the T17 test is greater than that in the H4 test, especially in the forward and lateral directions. This phenomenon corresponds to the velocity STD of two IMUs installed at different positions. In addition, we find that the error decrease difference between the two IMUs is mainly on that the position error of the velocity measurement model in the T17 test is larger than that of H4. This proves the velocity measurement model yields additional positioning errors when the vehicle vibrates. We can conclude that the distance increment measurement model is less sensitive to carrier vibrations and shows better robustness than the velocity model.

4.3.2. Emergency stops test

In the field tests, we designed two emergency stops in Group B to compare the robustness of the distance increment model. Emergency stops occurred at approximately 460,400 and 460760 s, respectively, and the speed curves are shown in Fig. 6. The GNSS outage test was performed in the emergency stop interval, and the position error aided by the two ODO/NHC measurement models was calculated. The horizontal position error curves are shown in Fig. 7.

As shown in Fig. 6, the speed changed too quickly to satisfy the linearity assumption when the robot stopped immediately. Consequently, the odometer speed measurement error increased. Therefore, the forward position error of the velocity measurement model increased sharply, as shown in Fig. 7. In contrast, the sudden speed change had no effect on the distance increment measurement accuracy. The forward position error of the distance increment model did not increase
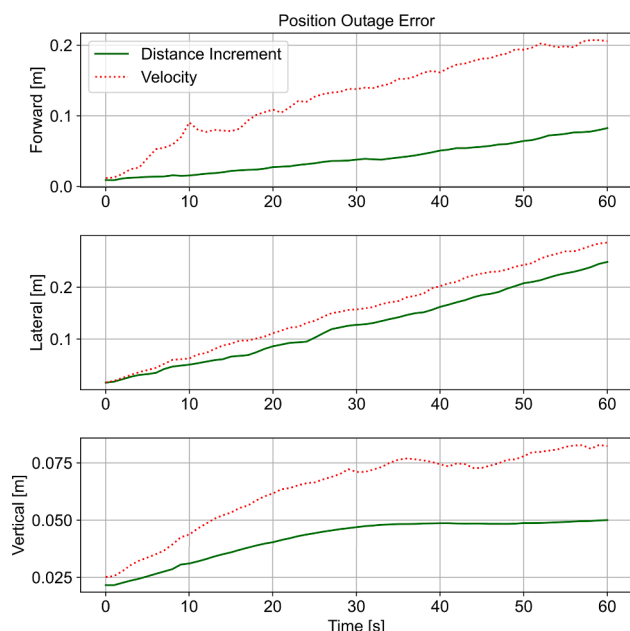

Fig. 5. Position error drift curves over outage time.

Table 4
Velocity STD of the IMUs Installed on the Tower (T17) and Board (H4).

IMU	Forward [m/s]	Lateral [m/s]	Vertical [m/s]
T17	0.036	0.015	0.0081
H4	0.031	0.0087	0.0082

Table 5

Position Errors of the IMUs Installed on the Tower (T17) and the Board (H4).

Test Group	Velocity Model [m]			Distance Model [m]			Error Decrease [%]		
	Forward	Lateral	Vertical	Forward	Lateral	Vertical	Forward	Lateral	Vertical
T17	0.294	0.324	0.084	0.082	0.240	0.054	72	26	36
H4	0.232	0.279	0.076	0.080	0.244	0.050	65	13	35
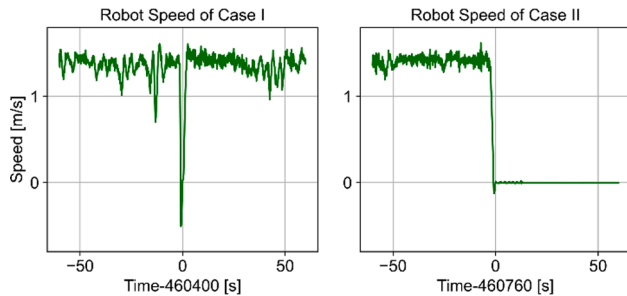
Fig. 6. Robot speed during of the emergency stops.

Fig. 7. Horizontal position errors of the emergency stops. The pink bands indicate GNSS outages.

Fig. 8. Passing speed bumps test scene.

Fig. 9. Velocity in the passing speed bumps test. Time passing the speed bump occur in the pink bands.

abnormally at emergency stops. In the lateral direction, position errors of both the two models increased slightly at the emergency stops. This was caused by a brief change in the IMU installation angles and odometer lever arm. In general, the distance increment model performs robustly in the case of emergency stops.

4.3.3. Passing speed bumps test

The passing speed bumps test was carried out in an open scene where the GNSS RTK positioning accuracy was at the centimeter level. The robot was driven back and forth to pass a manually placed speed bump with a height of approximately 8 cm, as shown in Fig. 8. In the test, the robot passed the speed bump six times. Fig. 9 shows the velocity of the robot.

During the test, the robot moved roughly east–west. The robot's speed in the forward direction (i.e., east direction) suddenly decreased when it passed the speed dump, as shown in Fig. 9. In addition, the speed bump caused a certain jolt to the robot, and the north and down speeds exhibited apparent fluctuations. The IMU installation angles and the odometer lever arm changed briefly but significantly when the two middle wheels passed the speed bump.

We conducted GNSS outage tests to evaluate the positioning performance of the two measurement models in the passing speed bumps test. The GNSS signal was interrupted for 10 s during the robot passing
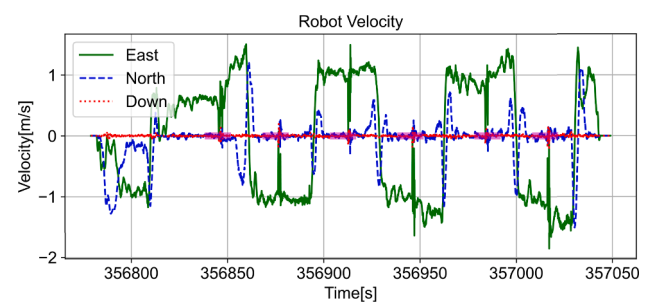
the speed bump. Subsequently, we calculated and compared the position errors using the two measurement models. The position errors of the two models in the passing speed bumps test are shown in Fig. 10.

In Fig. 10, when the robot passed the speed bump, the position errors of the velocity and distance increment measurement models increased significantly because of the change in the installation angles and lever arm. The instantaneous velocity measurement error will increase sharply if a change in the installation angles and lever arm occurs at that instant. The distance increment model is relatively insensitive to temporary changes in the installation angles and lever arm, considering it constrains the moving distance within a second. Consequently, the forward position error of the velocity model in the third and fourth outages was significantly larger than that of the distance increment measurement model. Although the velocity measurement model yielded a smaller forward position error in the last GNSS outage, the distance increment model exhibits a more accurate positioning result overall in the forward direction. In the lateral and vertical directions, the distance increment model's position errors are also obviously minor than the velocity model, confirming the necessity of extending NHC to distance increment constraint. Then, we counted the RMS values of the position errors in the two outage tests, as listed in Table 6.

According to Table 6, the position error reduction of the distance increment model compared with that of the velocity model is substantial. Specifically, the distance increment model has a position error reduction of 59 %, 38 %, and 41 % in the three directions of the v-frame, respectively. The statistical results of the passing speed bump tests
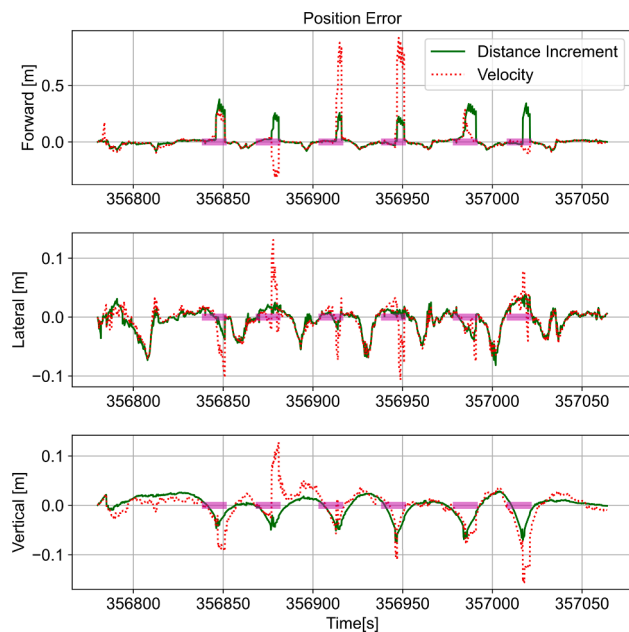
Fig. 10. Position error in the passing speed bumps test. The pink bands indicate GNSS outages.

Table 6
Position Errors in the Passing Speed Bumps Test.

Direction	Velocity Model [m]	Distance Model [m]	Error Decrease [%]
Forward	0.581	0.238	59
Lateral	0.098	0.061	38
Vertical	0.083	0.049	41

confirm the robustness of the ODO/NHC distance increment model. Additionally, the superior error decrease in the lateral direction than in Table 3 verifies that extending NHC to a distance increment constraint exhibits more robust positioning in such a harsh case.

Generally, the conducted navigation accuracy and robustness tests show that the ODO/NHC distance increment measurement model demonstrates better positioning accuracy and more robust performance than the velocity model in wheeled robot positioning.

5. Conclusion

In this study, the positioning accuracy and robustness of the ODO/ NHC velocity and distance increment measurement models dedicated for wheeled robot navigation were investigated in detail. Particularly, ODO/NHC distance increment measurement model was constructed in the three dimensions of the carrier frame, in which the NHC was also extended as a distance increment constraint. Then the measurement accuracy and the robustness of the two ODO/NHC measurement models were analyzed based on the motion characteristics of wheeled robots. Finally, adequate field tests were conducted to evaluate the positioning accuracy and robustness of these two ODO/NHC measurement models.

The theoretical analysis for the wheeled robot motions indicated that the ODO/NHC distance increment measurement yielded higher accuracy than the velocity measurement and was insensitive to rapid speed changes and carrier vibrations. Field test results proved that both the ODO and NHC distance increment measurement exhibited smaller measurement error and superior positioning accuracy for wheeled robots. Compared with the velocity model, the forward, lateral, and vertical positioning errors using the distance increment model decreased by 67 %, 15 %, and 39 %, respectively. Additionally, the distance increment

model outperformed the velocity model in terms of robustness in harsh cases, such as vibration, emergency stops, and passing speed bumps.

As wheeled robots can usually provide multi-odometer measurements of all wheels, including the steered wheels. Therefore, the use of distance increment measurement of all steered wheels and non-steering wheels for wheeled robot positioning will be the future research work.

CRediT authorship contribution statement

Liqiang Wang: Methodology, Software, Data curation, Validation, Writing – original draft. **Xiaoji Niu:** Conceptualization, Writing – review & editing, Supervision. **Tisheng Zhang:** Conceptualization, Writing – review & editing, Funding acquisition, Supervision. **Hailiang Tang:** Software, Data curation. **Qijin Chen:** Methodology.

Declaration of Competing Interest

The authors declare that they have no known competing financial interests or personal relationships that could have appeared to influence the work reported in this paper.

Data availability

Data will be made available on request.

References

[1] C.J. Hegarty, The Global Positioning System (GPS), in: P.J.G. Teunissen, O. Montenbruck (Eds.), Springer Handbook of Global Navigation Satellite Systems, Springer International Publishing, Cham, 2017, pp. 197–218, https://doi.org/10.1007/978-3-319-42928-1_7.

[2] N. El-Sheimy, A. Youssef, Inertial sensors technologies for navigation applications: state of the art and future trends, Satellite Navigation. 1 (2020) 2, https://doi.org/10.1186/s43020-019-0001-5.

[3] L. Wang, H. Tang, T. Zhang, Q. Chen, J. Shi, X. Niu, Improving the Navigation Performance of the MEMS IMU Array by Precise Calibration, IEEE Sensors J. 21 (22) (2021) 26050–26058, https://doi.org/10.1109/JSEN.2021.3118455.

[4] X. Li, X. Wang, J. Liao, X. Li, S. Li, H. Lyu, Semi-tightly coupled integration of multi-GNSS PPP and S-VINS for precise positioning in GNSS-challenged environments, Satellite Navigation. 2 (2021) 1, https://doi.org/10.1186/s43020-020-00033-9.

[5] P.D. Groves, Principles of GNSS, Inertial, and Multi-sensor Integrated Navigation Systems, 2nd ed.,, Artech House, 2013.

[6] G. Dissanayake, S. Sukkarieh, E. Nebot, H. Durrant-Whyte, The aiding of a low-cost strapdown inertial measurement unit using vehicle model constraints for land vehicle applications, IEEE Trans. Robot. Automat. 17 (2001) 731–747, https://doi.org/10.1109/70.964672.

[7] X. Niu, S. Nassar, N. El-Sheimy, An Accurate Land-Vehicle MEMS IMU/GPS Navigation System Using 3D Auxiliary Velocity Updates, Navigation. 54 (2007) 177–188, https://doi.org/10.1002/j.2161-4296.2007.tb00403.x.

[8] K.-W. Chiang, H.-W. Chang, Y.-H. Li, G.-J. Tsai, C.-L. Tseng, Y.-C. Tien, P.-C. Hsu, Assessment for INS/GNSS/Odometer/Barometer Integration in Loosely-Coupled and Tightly-Coupled Scheme in a GNSS-Degraded Environment, IEEE Sensors J. 20 (6) (2020) 3057–3069, https://doi.org/10.1109/JSEN.2019.2954532.

[9] B. Liang, Y. Qin, G. Yan, L. Peng, On Integrated Navigation for Vehicle Dead Reckoning, Computer, Measurement & Control. (2010). http://en.cnki.com.cn/Article_en/CJFDTOTAL-JZCK201010055.htm.

[10] Y. Zhou, Q. Chen, X. Niu, Kinematic Measurement of the Railway Track Centerline Position by GNSS/INS/Odometer Integration, IEEE Access 7 (2019) 157241–157253, https://doi.org/10.1109/ACCESS.2019.2946981.

[11] L. Li, H. Sun, S. Yang, X. Ding, J. Wang, J. Jiang, X. Pu, C. Ren, N. Hu, Y. Guo, Online calibration and compensation of total odometer error in an integrated system, Measurement 123 (2018) 69–79, https://doi.org/10.1016/j.measurement.2018.03.044.

[12] Q. Wang, M. Fu, Z. Deng, H. Ma, A comparison of loosely-coupled mode and tightly-coupled mode for INS/VMS, in: 2012 American Control Conference (ACC), IEEE, Montreal, QC, 2012: pp. 6346–6351. 10.1109/ACC.2012.6314914.

[13] Q. Fu, Y. Liu, Z. Liu, S. Li, B. Guan, High-Accuracy SINS/LDV Integration for Long-Distance Land Navigation, IEEE/ASME Trans. Mechatron. 23 (6) (2018) 2952–2962, https://doi.org/10.1109/TMECH.2018.2875151.

[14] S. Yousuf, M.B. Kadri, Sensor fusion of INS, odometer and GPS for robot localization, in: In: 2016 IEEE Conference on Systems, Process and Control (ICSPC), 2016, pp. 118–123, https://doi.org/10.1109/SPC.2016.7920715.

[15] Z. Zhang, X. Niu, H. Tang, Q. Chen, T. Zhang, GNSS/INS/ODO/wheel angle integrated navigation algorithm for an all-wheel steering robot, Meas. Sci. Technol. 32 (2021), 115122, https://doi.org/10.1088/1361-6501/ac17fb.

[16] N. Ganganath, H. Leung, Mobile robot localization using odometry and kinect sensor, in: 2012 IEEE International Conference on Emerging Signal Processing Applications, IEEE, Las Vegas, NV, USA, 2012: pp. 91–94. 10.1109/ESPA.2012.6152453.

[17] W. Ouyang, Y. Wu, H. Chen, INS/Odometer Land Navigation by Accurate Measurement Modeling and Multiple-Model Adaptive Estimation, IEEE Trans. Aerosp. Electron. Syst. 57 (1) (2021) 245–262, https://doi.org/10.1109/TAES.2020.3011998.

[18] Y. Wu, X. Niu, J. Kuang, A Comparison of Three Measurement Models for the Wheel-Mounted MEMS IMU-Based Dead Reckoning System, IEEE Trans. Veh. Technol. 70 (11) (2021) 11193–11203, https://doi.org/10.1109/TVT.2021.3102409.

[19] T.M. Howard, A. Kelly, Optimal Rough Terrain Trajectory Generation for Wheeled Mobile Robots, The International Journal of Robotics Research. 26 (2) (2007) 141–166, https://doi.org/10.1177/0278364906075328.

[20] P.G. Savage, Strapdown Inertial Navigation Integration Algorithm Design Part 1: Attitude Algorithms, Journal of Guidance, Control, and Dynamics. 21 (1998) 19–28, https://doi.org/10.2514/2.4228.

[21] Q. Chen, Q. Zhang, X. Niu, Estimate the Pitch and Heading Mounting Angles of the IMU for Land Vehicular GNSS/INS Integrated System, IEEE Trans. Intell. Transport. Syst. (2020) 1–13, https://doi.org/10.1109/TITS.2020.2993052.

[22] Q. Zhang, Y. Hu, X. Niu, Required Lever Arm Accuracy of Non-Holonomic Constraint for Land Vehicle Navigation, IEEE Trans. Veh. Technol. 69 (8) (2020) 8305–8316, https://doi.org/10.1109/TVT.2020.2995076.

[23] R.M. Rogers, Applied Mathematics in Integrated Navigation Systems, 2nd ed., Aiaa, Virginia, 2003.

[24] K.J. Wu, C.X. Guo, G. Georgiou, S.I. Roumeliotis, VINS on wheels, in, IEEE International Conference on Robotics and Automation (ICRA) 2017 (2017) 5155–5162, https://doi.org/10.1109/ICRA.2017.7989603.

[25] Xiaoji Niu, C. Goodall, S. Nassar, N. El-Sheimy, An Efficient Method for Evaluating the Performance of MEMS IMUs, in: 2006 IEEE/ION Position, Location, And Navigation Symposium, IEEE, Coronado, CA, 2006: pp. 766–771. 10.1109/PLANS.2006.1650673.